



A high efficient micro-proton exchange membrane fuel cell by integrating micro-nano synergical structures

Hsien-Chih Peng^a, Chung-Nan Wang^a, Tsung-Kuang Yeh^{a,c}, Yu-Chuan Su^a, Chin Pan^a, Fan-Gang Tseng^{a,b,*}

^a Department of Engineering and System Science, National Tsing Hua University, Hsinchu 30013, Taiwan, ROC

^b Division of Mechanics, Research Center for Applied Sciences, Academia Sinica, Nankang, Taipei 115, Taiwan, ROC

^c Nuclear Science and Technology Development Center, National Tsing Hua University, Hsinchu 30013, Taiwan, ROC

HIGHLIGHTS

- ▶ We fabricated a silicon-based micro-PEMFC performing an outstanding efficiency.
- ▶ The catalyst utilization ratio is superior to the currently reported micro-PEMFCs.
- ▶ The remarkable performance was due to the combination of three mechanisms.
- ▶ Enhanced reaction area, cell strength and cathodic efficiency are the mechanisms.
- ▶ We employed SEM, TEM, CV, EIS and Polarization Curves to verify the mechanisms.

ARTICLE INFO

Article history:

Received 3 July 2012

Received in revised form

15 September 2012

Accepted 18 September 2012

Available online 24 October 2012

Keywords:

Micro-fuel cell

Passive fuel cell

Membrane electrode assembly

Carbon nano-tube

Three-phase zone

ABSTRACT

A silicon-based micro-proton exchange membrane fuel cell (μ -PEMFC) which carries out an outstanding cell performance and high efficient catalyst utilization ratio is proposed in this paper by the employment of three micro-nano synergical techniques. Firstly, a novel design incorporating multi-walled carbon nano-tubes (MWCNTs) on radial shaped micro-channel walls to form micro/nano reaction chambers which significantly enhance the reaction surface areas for the performance improvement. In the second, the dispensing of ionomer onto the three-phase zones in the reaction chambers is controlled by different rotation speed and the optimized distribution can therefore be achieved for the improvement of catalyst utilization. In the third, the cell interfacial strength is greatly enhanced by the employment of micro-interlocks for maintaining excellent interface between Nafion membrane and reaction chambers while minimizing the system size. A μ -PEMFC is successfully fabricated by integrating aforementioned synergical micro/nano structures altogether. The best cell efficiency is 26 mW cm^{-2} which corresponds to a catalyst utilization ratio of $38.2 \text{ W g}_{\text{Pt}}^{-1}$ and can be considered among the best performed micro-fuel cells.

Crown Copyright © 2012 Published by Elsevier B.V. All rights reserved.

1. Introduction

Portable power supply systems could potentially provide an alternative energy source for portable electronic devices such as smart phones or laptops. According to the low temperature start-up feature, proton exchange membrane fuel cells (PEMFCs) and direct methanol fuel cells (DMFCs) could be the solutions. Typically, the configuration of both the PEMFCs and DMFCs consists of membrane

electrode assembly (MEA) and flow channel plates, and the MEA usually consists of Nafion membrane, anodic and cathodic catalyst layers, gas diffusion layers. A single cell can be accomplished by sandwiching the flow channel plates and MEA together. However, the flow channels are usually made of graphite and result in a bulky system, which is not favorable to the portable devices. Moreover, limited by the configuration of the MEA, the catalyst layers are usually allocated in a two-dimensional plane, not a three-dimensional structure; therefore, the total surface reaction areas will also be limited.

To overcome the limitations, MEMS technology was employed to the fabrication of monolithic micro-MEA (μ -MEA) for micro-proton exchange membrane fuel cells (μ -PEMFCs) and micro-

* Corresponding author. Department of Engineering and System Science, National Tsing Hua University, 101, Sec. 2, Kuang-fu Rd., Hsinchu 30013, Taiwan, ROC. Tel.: +886 3 5715131 34270; fax: +886 3 5733054.

E-mail address: fangang@ess.nthu.edu.tw (F.-G. Tseng).

Table 1

The comparison of the performance with the present micro-PEMFCs and DMFCs.

Author	Method	Type	Anode	Cathode	Best peak power density (mW cm^{-2})	Total catalyst loading ($\text{mg}_{\text{Pt}} \text{cm}^{-2}$)	Catalyst utilization ratio ($\text{W g}_{\text{Pt}}^{-1}$)
K. Shah et al. [1]	μ -Structures μ -fluidic channels	PEMFC	Active H_2	Passive air	0.3	0.014	29
Y. Zhang et al. [2]	μ -Structures μ -fluidic channels	DMFC	Active MeOH	Passive air	0.025	—	—
K.B. Min et al. [3]	μ -Fluidic channels	PEMFC	Active H_2	Passive air	0.09	—	—
S.C. Kelly et al. [4]	μ -Structures	PEMFC	Active H_2	Active O_2	125	3.5	35
J. Yeom et al. [5]	μ/n -Structures	PEMFC	Active H_2	Active O_2	35	5	7
J. Yeom et al. [6]	μ/n -Structures	PEMFC	Active H_2	Active O_2	54	5	10.8
Z. Xiao et al. [7]	μ -Structures	PEMFC	Active H_2	Active O_2	13.7	0.43	16
		DMFC	Active MeOH	Passive air	0.21	0.43	0.24
Y. H. Seo et al. [8]	μ -Structures	DMFC	Active MeOH	Passive air	0.02	—	—
This study	μ/n -Structures μ -interlocks Spinning-in process	PEMFC	Active H_2	Active O_2	26	0.68	38.2

direct methanol fuel cells (μ -DMFCs) [1–8]. By using the MEMS technology, bulky flow channels can be replaced by the micro-fabricated flow channels, and the catalyst layers can be deposited onto the Nafion membrane by the micro-modified structures [1,2] for μ -PEMFCs. K. Shah et al. [1] integrated a polydimethylsiloxane (PDMS) based micro-flow channels and micro-patterned Nafion[®] with thin catalyst layers to fabricate a μ -PEMFC, and perform a maximum power density of 0.3 mW cm^{-2} at 60°C . Similarly, Y. Zhang et al. [2] proposed a μ -PEMFC by assembling silicon based micro-flow channels and micro-imprinted laminated Pt/Nafion[®] films, and showed a maximum power density of 2.3 mW cm^{-2} at 60°C . According to the study of K. B. Min et al. [3], a μ -PEMFC can be carried out in either inverted or co-planed form, depending on the different packaging needs. Moreover, Pt catalyst layers can also be integrated in a 3-dimensional configured micro-channeled chip set. The inverted form showed the best performance of 0.09 mW cm^{-2} at room temperature with a Pt loading of 0.43 mg cm^{-2} . However, a co-planed design seems to have lower power density at 0.04 mW cm^{-2} when compared to that of the inverted form.

Besides, the reaction surface areas can be significantly increased by three-dimensional micro- and nano-arrayed configurations [4–8]. Kelly et al. [4] first demonstrated a silicon based μ -MEA with dense micro-hole array by MEMS process. The optimal power density was 125 and 15 mW cm^{-2} as a μ -PEMFC and μ -DMFC, respectively, and the total Pt loading was in a range from 3.5 to 3.78 mg cm^{-2} . J. Yeom et al. [5,6] also demonstrated a micro- and nano-structured μ -MEA. This design incorporated nano-scaled dendritic Pt catalysts in micro-scaled reaction hole array to enhance the reaction surface areas, and the total catalyst loading was 5 mg cm^{-2} . It produced a maximum power density of 54 and 0.38 mW cm^{-2} as μ -PEMFC and μ -DMFC, respectively. In contrast to micro-hole array, silicon micro-column array was also employed to the silicon based μ -MEAs. Z. Xiao et al. [7] proposed a textured silicon μ -MEA, which generates the maximum power density of 13.7 and 0.21 mW cm^{-2} for μ -PEMFC and μ -DMFC, respectively. The total catalyst loading in a single cell was 0.86 mg cm^{-2} . Moreover, a similar concept for μ -DMFCs was also presented by Y.H. Seo et al. [8], and a maximum power density of 0.07 mW cm^{-2} was reported.

Table 1 compares the detailed parameters and performances of the aforementioned papers. The authors used different MEMS-based techniques for building up high performance μ -fuel cells. However, rarely the studies integrate more than two efficiency-facilitating components in their research, and the performance of catalyst

utilization ratio is limited to $35 \text{ W g}_{\text{Pt}}^{-1}$. Therefore, the strategy in this study is to integrate three MEMS-based techniques to increase reaction surface area, improve contact interface, and reduce oxygen transportation path, respectively, for overall performance enhancement.

2. Design and fabrication

2.1. Micro-fuel cell design

The detailed design is schematically shown in Fig. 1. First, according to Table 1, micro- and nano-structures were the most efficient method to enhance the reaction surface area. In this study, we employ micro- and nano-synergized structures for increasing reaction surface area by incorporating multi-walled carbon nanotubes (MWCNTs) into micro-structures. A 3.5 orders of surface area increment, as compared to the flat silicon surface, can therefore be obtained.

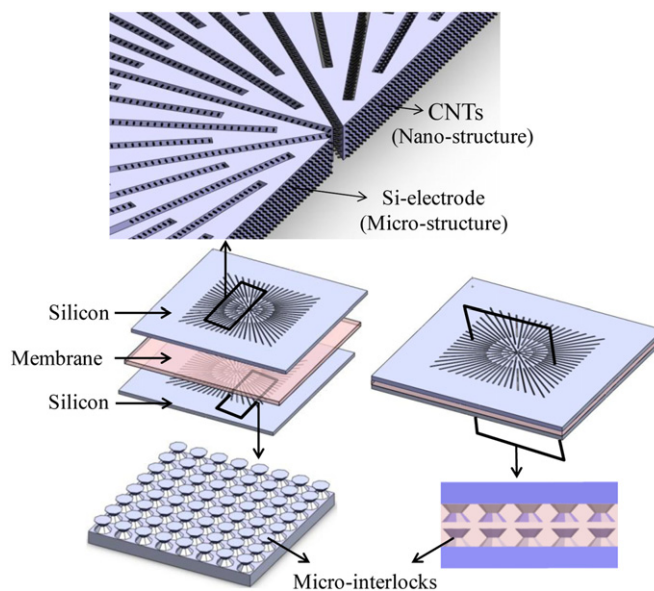
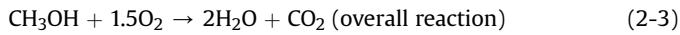
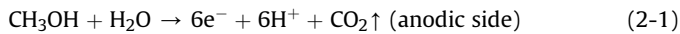
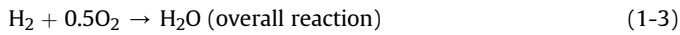
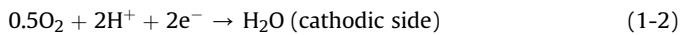


Fig. 1. The schematic diagram of the μ -PEMFC, which consists of radial type micro- and nano-structured electrodes and micro-interlocks.

In the second, the interfacial strength between bipolar plates and Nafion membrane is enhanced by employing self interlocking structures between them. Actually, a low interfacial strength poses high contact impedance at the junction of bipolar plates and Nafion membrane, and a minimum clamping stress of about 2 MPa is typically required [9]. K. B. Min et al. [3] also gave a supporting data showing that a better reliability of micro-fuel cells can be achieved by equipping with an external clamping system. Accordingly, the higher the interfacial strength not only lowers the ohmic impedance but also eases the dependence on additional clamping systems. According to our earlier research, micro sandglass shaped interlocks with surface nano-structures provided a highest interfacial strength of 3.2 MPa at the interface of silicon substrates and Nafion membrane [10], which is sufficient for the interfacial strength requirement of micro-fuel cells.

In the third, according to Table 1, the power density was apparently low when the cathodes were operated under a passive (air-breathing) condition. Therefore, the major hurdle to the performance could come from the cathodic efficiency.

Equations (1-1)–(1-3) representing the reactions of PEMFCs, and equations (2-1)–(2-3) representing the reaction of DMFCs,



We can find that the cathodic reactions of both the fuel cell types are similar to each other. Since the oxygen reduction reaction (ORR) takes place at the interface among catalysts, oxygen and Nafion membrane, so called three-phase zones [11,12], the oxygen diffusivity in ionomer is crucial to the cathodic efficiency. As

a result, ionomer is usually employed as the bridge between electrodes and Nafion membrane. However, in the micro-system, due to capillarity effect, ionomer always inevitably clogs the micro-holes from spraying dispensing process, hence impedes the oxygen diffusion and deteriorates the ORR, and leaves some catalysts inactive. Therefore, a low catalyst utilization ratio ($W_{\text{g-pt}}^{-1}$ dividing the power density, mW cm^{-2} , by the catalyst loading density, $\text{mg}_{\text{-pt}} \text{cm}^{-2}$) can be anticipated. Accordingly, this could be one of the reasons why the micro-fuel cell's performance is so sensitive to the cathodic reaction. To reduce oxygen diffusion impedance, the thickness of ionomer in the reaction site should be well controlled.

In order to enhance the ORR and catalyst utilization ratio simultaneously, the third method employed is to control the ionomer thickness by spin-coating process into radial type reaction chambers. The surplus ionomer can therefore be removed from the reaction chamber along the radial direction due to centrifugal force. Thus, the oxygen diffusion path can be ventilated, and more Pt catalysts deep inside the reaction chamber will have a higher possibility to be contacted by oxygen.

2.2. Device fabrication

Fig. 2 shows the fabrication process flow of the micro-fuel cell. We first grew 1 μm silicon oxide (SiO_2) layer on both sides of a 230 μm -thick-silicon wafer. A 7 μm -tall silicon posts array covered with SiO_2 hard mask was then fabricated by a sequential photolithography and deep silicon reactive ion etching (DRIE) processes (Fig. 2(a)–(c)). A micro-interlocks array was fabricated after a 32 wt.% KOH etching for 1.5 min at 80 $^\circ\text{C}$ (Fig. 2(c)). Here, the micro-interlocks serve as the reinforcing structures at the interface between silicon-based electrodes and Nafion membrane [10]. A radial shaped reaction chamber was accomplished by photolithography and DRIE processes, consecutively (Fig. 2(e) and (f)). Layers of thin metal films were then deposited on the sidewalls of micro-reaction chamber by sputtering deposition, and the sequence of the metal layers is Ti (300 \AA), Al (1000 \AA), Ti (300 \AA) and Ni (200 \AA). Here, Ti, Al and Ni layers serve as the adhesion, electron conduction and multi-walled carbon nano-tubes

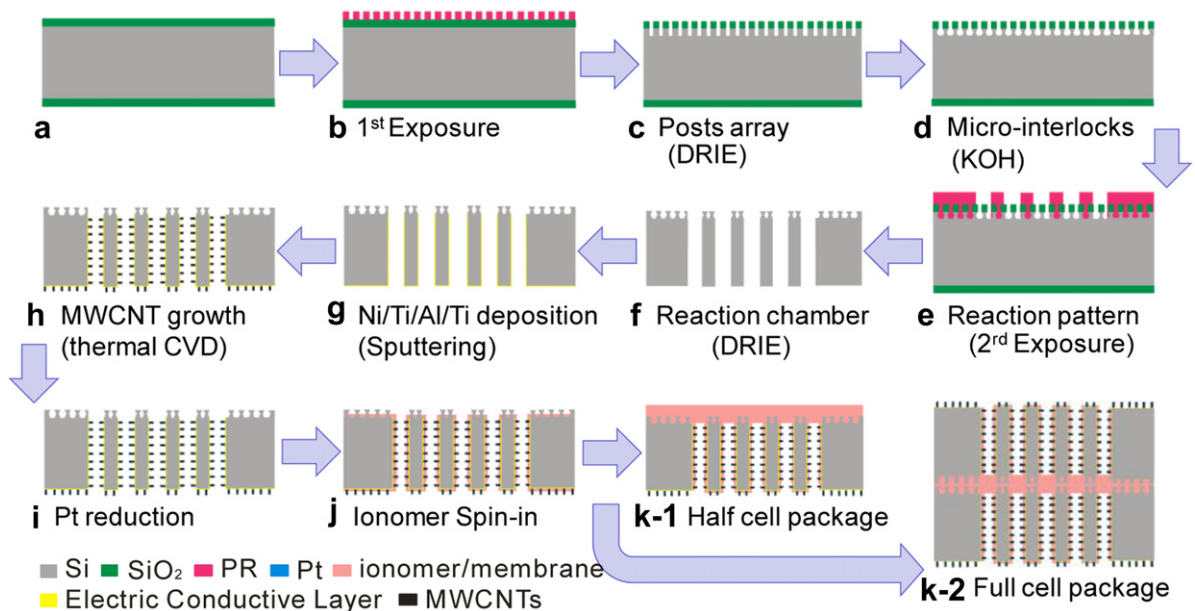


Fig. 2. Fabrication process of the μ -MEAs. (a) Silicon wafer with 1 μm oxide layer; (b) pillar array definition; (c) 7- μm tall posts array fabrication by DRIE; (d) micro-interlocks fabrication by KOH etching; (e) radial shaped reaction area definition; (f) reaction area fabrication by DRIE; (g) thin metal layers deposition by sputtering; (h) MWCNTs growth; (i) Pt catalysts reduction; (j) ionomer spin-in; (k-1) half cell package; (k-2) full cell package.

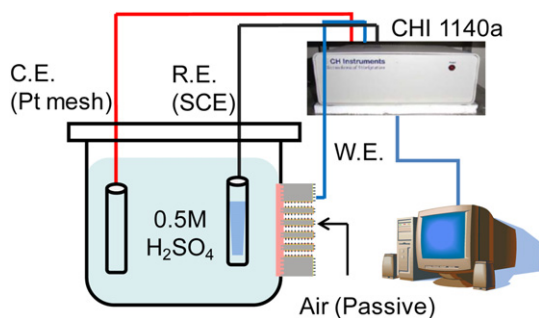


Fig. 3. The half cell testing system: reference electrode (RE) and counter electrode (CE) are connected to a saturated calomel electrode (SCE) and a Pt mesh, respectively. For the testing specimen, structure side of the μ -half MEA is exposed to the air, while the membrane (Nafion[®]117) side is contacted the 0.5 M H_2SO_4 solution.

(MWCNTs) catalytical layers, respectively (Fig. 2(g)). After MWCNTs formed inside the reaction chamber on the substrates by chemical vapor deposition (CVD, Fig. 2 (h)), catalysts for electrochemical reaction (Pt) were deposited on MWCNTs by an open-loop reduction process, and the diameter of the catalysts was about 3–5 nm [13] (Fig. 2(i)). Drops of 5% and 20% ionomer were then dispensed into the reaction chamber, consecutively, and followed by a spinning-in process to control the thickness of ionomer on the MWCNTs. Note that the 5% ionomer drop was first employed to wetting the MWCNTs for better 20% ionomer coating later. The spinning-in conditions were 1000, 2000, 3000 and 4000 rpm in this study (Fig. 2(j)). Finally, a micro-half-MEA for cathodic test was completed by assembling Nafion membrane (Nafion[®] 117) and cathode at 2 MPa and 125 °C for 3 min (Fig. 2(k-1)). For full cell testing, a μ -MEA was accomplished by assembling anode, Nafion membrane (Nafion[®] 115) and cathode at 2 MPa and 125 °C for 3 min (Fig. 2(k-2)).

2.3. Experiments

The micro-scaled structural profiles were observed by FE-SEM (JEOL JSM-6330F) and the nano-scaled features were identified by TEM (JEOL, JEM-2010) images. The loading mass of Pt supported on MWCNTs was measured by inductively coupled plasma-mass spectrometer (ICP-MS, Perkin Elmer, SCIEX ELAN 5000). The half cell efficiency was estimated by current–voltage curves (CV curves) and electrochemical impedance spectrum (EIS). The full cell efficiency was obtained from polarization curves by the Chronopotentiometry of Current Ramp method. Both the half and full

cell testing were carried out by using an electro-chemical workstation (CHI 1140a, CH Instruments, Inc, USA), which provides three-electrodes including working electrode (WE), reference electrode (RE) and counter electrode (CE). The electrochemical impedance spectrum (EIS) for half cell was examined by the other electro-chemical workstation (AUTOLAB PGSTAT302). Fig. 3 schematically shows the setup for the half cell testing. The structural side of the micro-half MEA was exposed to the air, namely a passive condition, and connected to the WE while the membrane side was contacted with the diluted sulfuric acid solution (0.5 M H_2SO_4). The RE and CE were connected to a saturated calomel electrode (SCE) and a Pt mesh, respectively. For CV curve measurement, WE bias was scanned from 0.9 V to 0.25 V, and for EIS measurement, the DC bias was set to 0.01 V and the frequency was scanned from 0.1 to 10 kHz. Fig. 4 shows the full cell testing scenarios for active and passive conditions. Layers of Ti (500Å) and Au (1500Å) for electron conduction were deposited on the acrylic plate by electron beam evaporation, consecutively, and all the screws and nuts were electrically insulated from the specimens and fixed at 0.5 kgf. Fig. 5(a) shows the real size of the μ -MEA, and the projection area is only 1 cm²; (b) shows the real size of the testing system, which is comparable to an AA battery. The current scan rate was 1×10^{-2} mA s⁻¹, and the scanning stopped when cell voltage approached 0.2 V. Both active and passive test were carried out in the current experiments. The flow rate of the hydrogen at the anode was 20 ml min⁻¹ for both active and passive system. On the other hand, the flow rate of the oxygen at the cathode was 40 ml min⁻¹ for active test only, and the cathode side was exposed to air during the test for passive system. Note that all the specimens for half and full cell test were activated in boiling de-ionized water (D. I. water) for 1 h, and preserved in D. I. water at room temperature for 24 h before tests. All the tests were operated at room temperature.

3. Results and discussion

3.1. SEM and TEM observation

Fig. 6 shows the top-view and side-view images of the micro- and nano-structured electrodes. Fig. 6(a) is the top-view image of an electrode, the detail of the central and peripheral is shown in (b) and (c), respectively, and the micro-interlocks can be clearly identified. Fig. 6(d) shows the cross-sectional images, the height of the micro-structure is about 250 μm . The length of the MWCNTs covering the sidewalls of the structures is in a range from 3 μm to 13 μm . By the combination of micro- and nano-structures, about 3.5 orders of magnitude surface area enhancement could be achieved.

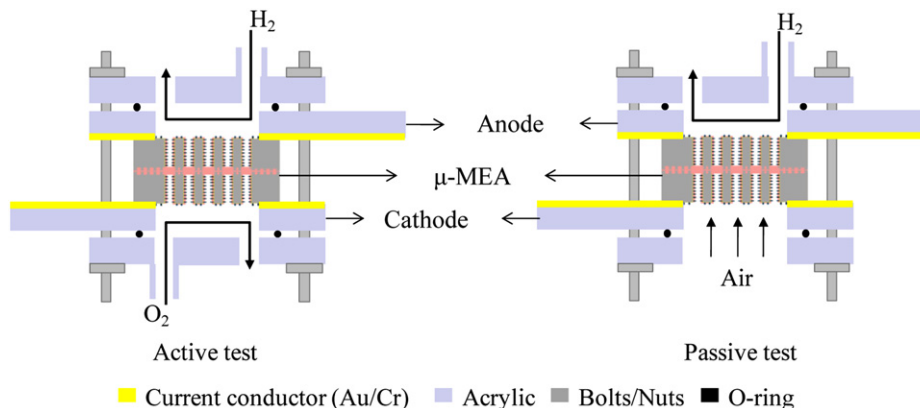


Fig. 4. The schematics of the active and passive full cell testing system.

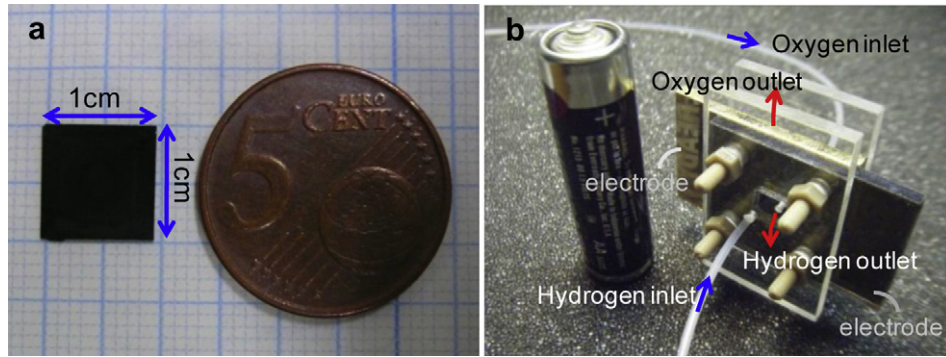


Fig. 5. (a) The optical image of μ -MEA: the projection area is only 1 cm^2 . (b) The actual full cell testing system, which is comparable to an AA battery.

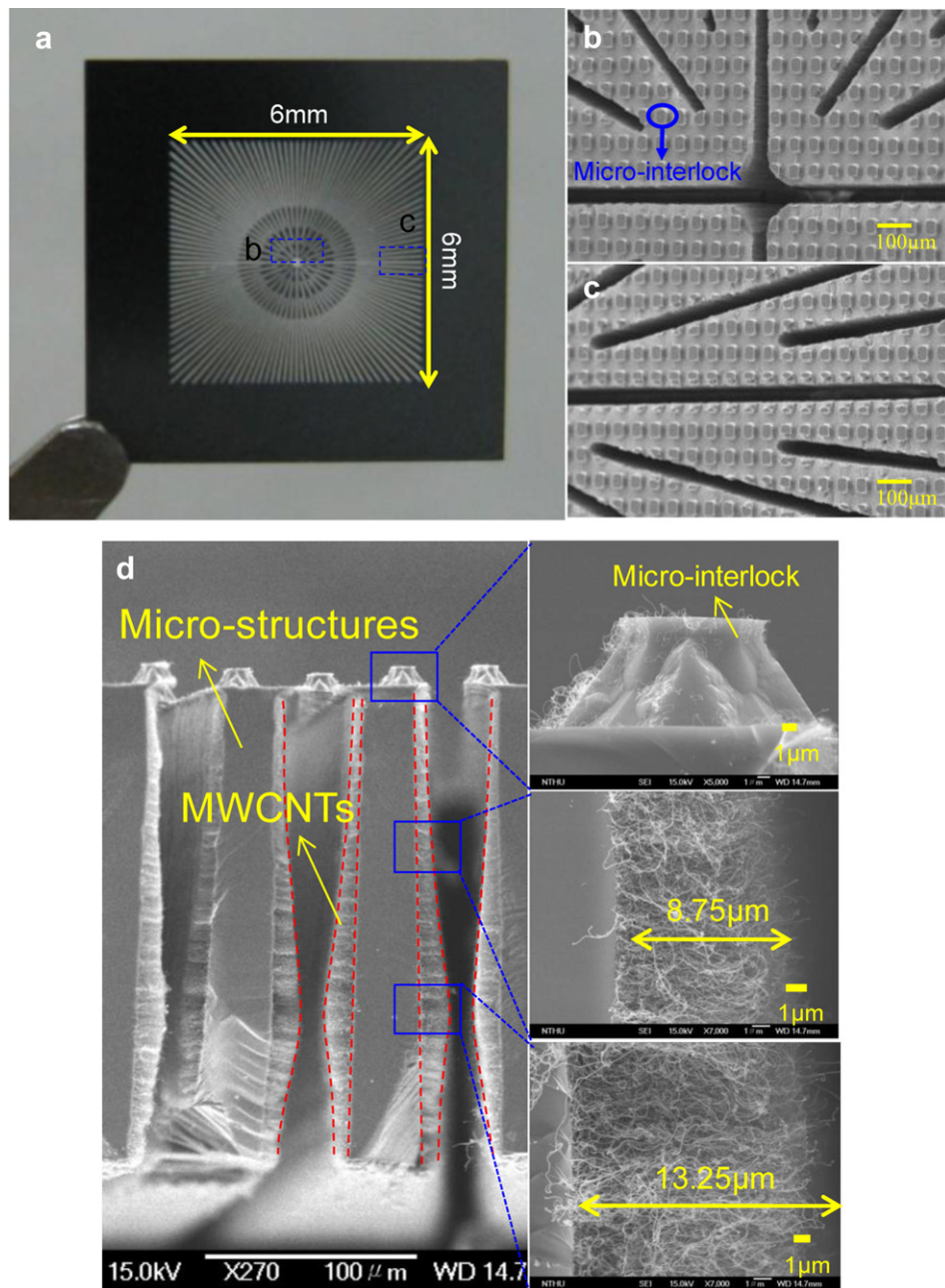


Fig. 6. The optical and SEM images of the micro-electrode for μ -PEMFCs. (a) Top view optical image. (b) and (c) Top view SEM images of the central and peripheral area on the micro-electrode, respectively. (d) Cross-sectional SEM image, the distribution of MWCNTs on the reaction chamber walls can be clearly observed.

The micro-interlocks are distributed uniformly over the electrode, and the height is about 8 μm .

We first compare the difference among the specimens which processed with and without spinning-in procedure, and then observe the distribution of ionomer in the micro-scale. Fig. 7(a) and (b) shows the schematics and the SEM images of the ionomer in the structure right after dispensing ionomer without and with the spinning-in process (1000 rpm), respectively. As a result, the clogging phenomena in micro-reaction chamber can be eliminated by a spinning-in process [14]. We thereby verify the distribution of ionomer inside the nano-structure under different rotation speeds at 1000, 2000, 3000 and 4000 rpm, respectively. The detailed PSFA distribution on the MWCNTs is then observed by TEM. Fig. 8 shows the TEM images of the MWCNTs after priming the ionomer by the spinning-in process, and the dark spots on the MWCNTs are the Pt catalysts. Fig. 8(a) shows the 1000 rpm case, and the ionomer is still thick enough to bridge most of the MWCNTs, while a thin layers of ionomer can be observed in 2000 rpm and 3000 rpm cases as 10 nm and 5 nm respectively, as shown in Fig. 8(b) and (c). The red arrows indicate some three-phase zones exposed to the ambient. ORR could take place without the oxygen diffusing through the ionomer at where indicated by red arrows. However, in 4000 rpm case, although a much thinner ionomer layer can be achieved, a discontinuous ionomer layer is also observed, and some catalysts are therefore isolated, as indicated by the green arrows in Fig. 8(d). From the TEM images, the higher the spinning-in condition shows a qualitatively better performance. In order to get quantitatively evidence, a series of cathodic micro-half-MEAs testing are performed. (For interpretation of the references to color in this paragraph, the reader is referred to the web version of this article.)

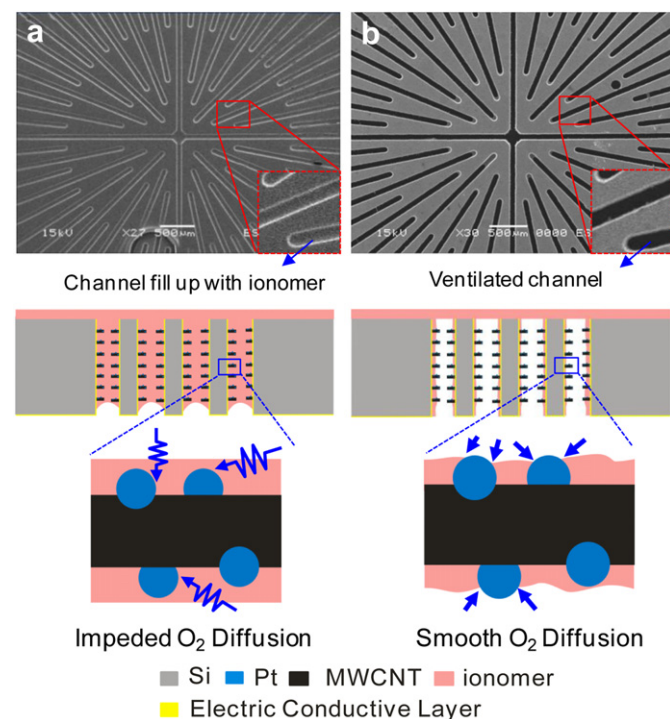


Fig. 7. The SEM images and schematics of the ionomer in the micro-electrode. (a) Specimen processed without spin-in procedure, and ionomer fills up the channel and clogs the oxygen diffusion path. (b) Specimen processed with spin-in (1000 rpm), and the channels were ventilated. The blue arrows in (b) indicate the three-phase zones exposed to the ambient. (For interpretation of the references to color in this figure legend, the reader is referred to the web version of this article.)

3.2. Half cell tests

Fig. 9 shows the micro-half-MEAs CV testing results. The black, blue, red and purple lines represent the spinning-in conditions of 1000, 2000, 3000, and 4000 rpm, respectively. The peak current densities are -8 , -32.5 , -42.5 , and -3 mA cm^{-2} of the 1000, 2000, 3000 and 4000 rpm spinning-in conditions, respectively. From 1000 to 3000 rpm, the higher cathodic efficiency corresponds to the higher spin rate, and this trend could be related to thinner ionomer layers on MWCNTs revealed in Fig. 8(a)–(c). Thinner ionomer provides a shorter oxygen diffusion path and thus improves the cathodic reaction efficiency. Although a much thinner ionomer on MWCNTs is observed when the spin rate is at 4000 rpm; however, the current density suddenly falls down under this condition. From Fig. 8(d), the discrete ionomer layer which could result in catalysts isolation, thus deteriorates the transportation of protons and catalyst utilization ratio. Actually, a minimum thickness of 4–6 nm water absorbed ionomer layer is generally required for the proton transportation [15,16]. The discontinuity could also influence the proton transportation. (For interpretation of the references to color in this paragraph, the reader is referred to the web version of this article.)

CV testing data shows the influence of the spinning-in process on the cathodic efficiency and an optimized condition can also be observed. However, the mechanism needs to be further verified; therefore, we employ EIS to find out the mechanism. Usually, a corresponding equivalent circuit is brought into the analysis. For the cathodic reaction, Ciureanu and Roberge [17] proposed an equivalent circuit for the cathode including ohmic resistance, charge transfer resistance for high and middle frequency regions, respectively, and diffusion resistance for low frequency region. Capacitors for double layers were considered in both the middle and low frequency regions. Furukawa et al. [11] also proposed a similar model for the cathodic impedance analysis. The same concept is employed in this study. Fig. 10 shows the equivalent circuit and the related physical model for this study. R_{ohm} represents the ohmic resistance, which reflects the impedance of hydrogen proton transported from dilute sulfuric acid to the three-phase zones. The pathway includes the Nafion® 117 and the baked ionomer inside the MWCNT-array. R_{ct} and C_{ct} represent the charge transfer resistance and capacitance, respectively. R_{ct} expresses the transferring impedance of the electrons from the reactants to the products at the three-phase zones. Since the reaction only takes place at the three-phase zones, surplus charges could accumulate and result in the effective capacitance (C_{ct}) at the three-phase zones. R_{diff} and C_{diff} represent the diffusion resistance and capacitance, respectively. R_{diff} reflects the impedance of oxygen gas diffusing from the ambient to the three-phase zones; similarly, the surplus oxygen could also possibly, even though at a very low possibility, accumulates at the three-phase zones and results in the effective capacitance (C_{diff}).

Fig. 11 shows the EIS testing results, solid lines and hollow squares lined by dots represent the simulation fitting and experimental data, respectively. The simulated data fits well to the experimental data, and the spectrum shows the same trend as the CV testing results. The values of the corresponding equivalent circuit elements are shown in Table 2.

At the low frequency region, oxygen diffusion dominates the reaction. According to Fig. 8(a)–(c), for the higher spin rate, the diffusion length of oxygen could be reduced owing to the thinner ionomer. In addition, more three-phase zones exposed to the ambient when the higher spin rate is applied, part of oxygen could approach three-phase zones without any diffusion process. Therefore, in this case, R_{diff} drops when the spin rates get higher from 1000 to 3000 rpm. However, even though a much thinner

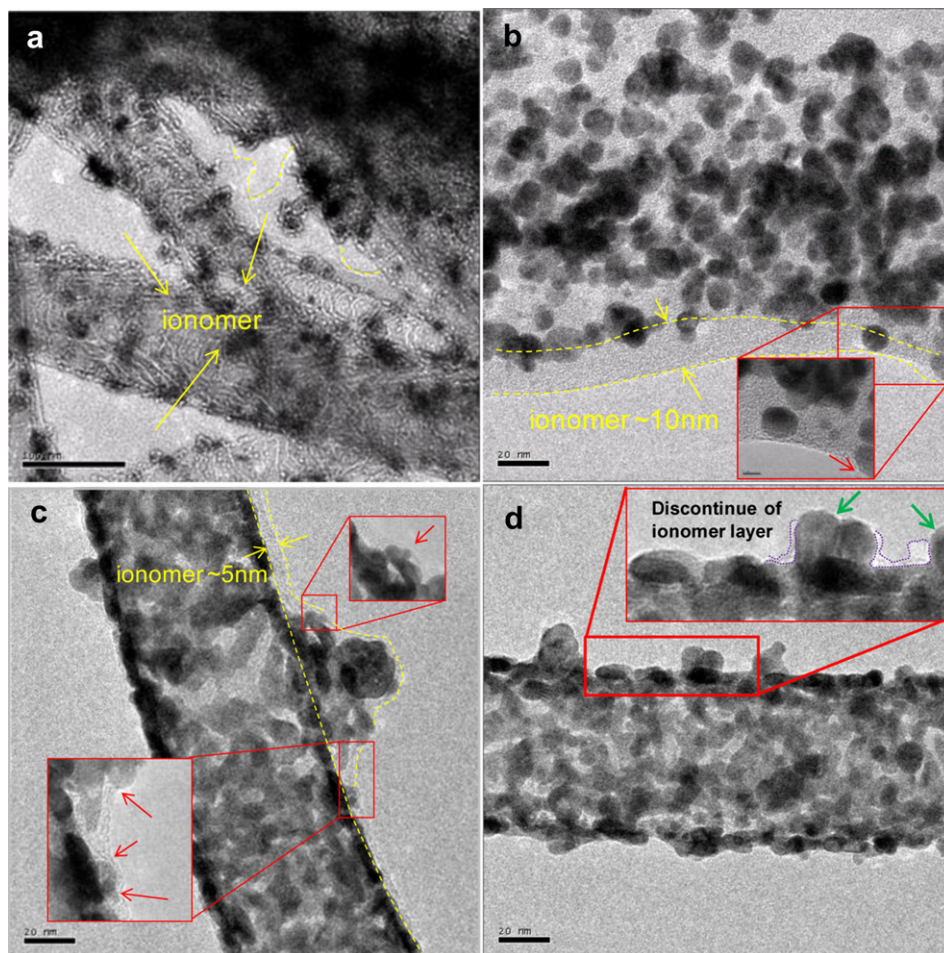


Fig. 8. TEM images of the MWCNTs with different ionomer spinning-in conditions; (a) 1000 rpm, (b) 2000 rpm, (c) 3000 rpm, and (d) 4000 rpm. The red arrows indicate some three-phase zones exposed to the ambient and the green arrows indicate the isolated catalysts. (For interpretation of the references to color in this figure legend, the reader is referred to the web version of this article.)

ionomer layers could be obtained at 4000 rpm spinning-in condition, owing to the massive inactive catalysts being observed, the current density at cathode could be highly localized, as result of a high charge transfer resistance on the catalyst surface of this

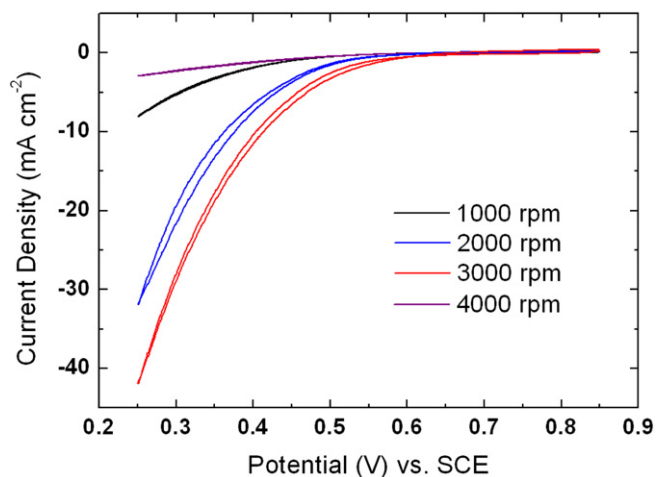


Fig. 9. The CV testing results of micro-half-MEAs; the black, blue, red and purple lines represent the spinning-in conditions of 1000, 2000, 3000, and 4000 rpm. (For interpretation of the references to color in this figure legend, the reader is referred to the web version of this article.)

ionomer. Thus, R_{diff} rises dramatically, instead. At the middle frequency region, charge transfer dominates the reaction. Here, R_{ct} also decreases with the increasing spin rate, and we can conclude that the thickness controlled ionomer layer not only facilitates the oxygen diffusivity but also enhances the charge transfer efficiency. Since various solvents in ionomer could result in the different performance in charge transfer impedance [18], the residual solvent could inevitably influence the R_{ct} . In this case, the residual solvent in the ionomer film should be more than that at the surface. Therefore, R_{ct} could be lowered when the reaction takes place at the

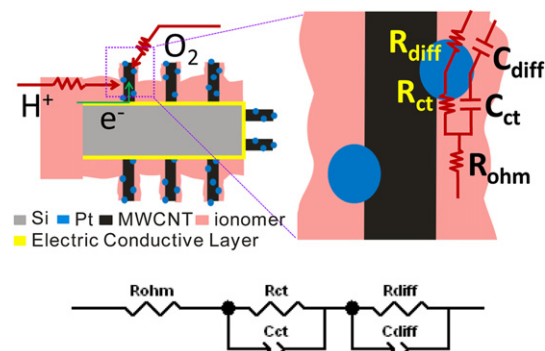


Fig. 10. The effective electric circuit and the corresponding physical model of the silicon based micro-half-MEA.

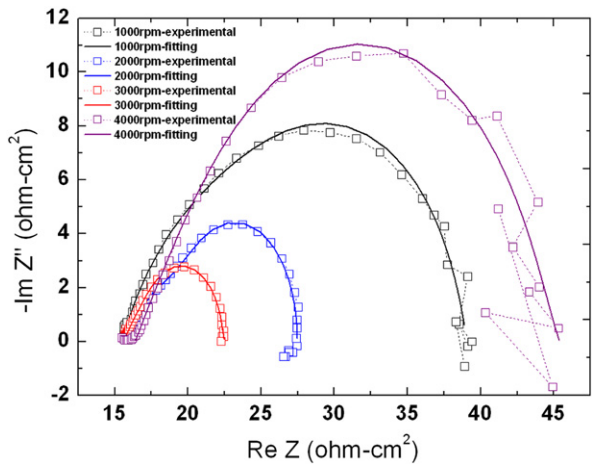


Fig. 11. The EIS testing results of micro-half-MEAs; the black, blue, red and purple represent the spinning-in conditions of 1000, 2000, 3000, and 4000 rpm, respectively. The solid lines and hollow squares lined by dots represent the simulation fitting and experimental data, respectively. (For interpretation of the references to color in this figure legend, the reader is referred to the web version of this article.)

three-phase zones exposed to the ambient. This could be the reason why R_{ct} reduces as the ionomer film thickness reduced. Fig. 12 schematically explains the phenomena.

At the high frequency region, the spectrums are nearly the same for each experimental condition. Since R_{ohm} dominates the reaction at high frequency, we can consider the impedance of the moving path of the hydrogen protons only. Actually, hydrogen proton should transport through the Nafion® 117, the interface between Nafion® and the structured silicon electrodes, and the ionomer on MWCNTs. For the traditional MEA, the interface is usually between carbon cloth and Nafion membrane, and R_{ohm} is usually below $1 \Omega \text{ cm}^{-2}$. Note that although micro-interlocks provide a high interfacial strength for this system; however, in this study, the proton conductivity at the interface between Nafion membrane and structured silicon electrodes probably still lower than that between Nafion membrane and structured carbon cloth. Therefore, the interfacial property is suggested dominating R_{ohm} rather than Nafion® 117 nor ionomer on MWCNTs. The performance can be enhanced by further improving the interface in the future.

3.3. Full cell tests

The cathodic CV and EIS testing results show convictive results that the cathodic efficiency of micro-fuel cells can be promoted by the unique process. Furthermore, the catalyst utilization ratio and the peak power density would be verified by polarization curves. Fig. 13(a) and (b) shows the polarization curves for active and passive testing results, respectively. The black square, blue pentagon, red hexagon and purple triangle represent the spinning-in conditions of 1000, 2000, 3000, and 4000 rpm, respectively. (For

Table 2
The simulated values of the equivalent circuit elements at the cathodes of this study.

Spin rate (rpm)	R_{ohm} ($\Omega \text{ cm}^2$)	R_{ct} ($\Omega \text{ cm}^2$)	R_{diff} ($\Omega \text{ cm}^2$)	CPE_{ct-T}	CPE_{ct-P}	CPE_{diff-T}	CPE_{diff-P}
1000	15.51	13.15	10.42	2.3×10^{-3}	0.7	2.9×10^{-3}	0.96
2000	16.01	5.04	6.5	1.8×10^{-3}	0.7	1.4×10^{-3}	1
3000	15.62	2.32	4.49	8.5×10^{-3}	0.67	3.3×10^{-3}	1
4000	16.1	13	16.01	5.8×10^{-3}	0.59	1.5×10^{-3}	0.98

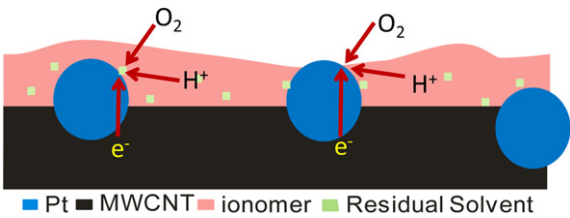


Fig. 12. The effect of residual solvent on the charge transfer impedance. The Pt catalysts residing inside the ionomer could absorb the residual solvent, and charge transfer process could be retarded; in contrast, the solvent evaporated when Pt catalysts exposed to the ambient, and the charge transfer impedance could be lowered.

interpretation of the references to color in this paragraph, the reader is referred to the web version of this article.)

Under the active testing condition, since hydrogen fuel is actively fed into anode and oxygen gas is forced into the cathode, the cathodic product, H_2O , can be removed accordingly. Therefore, none of the concentration polarization is observed in every condition.

Under the passive testing condition, the concentration polarization is not observed when the spin rate is higher than 1000 rpm. According to Fig. 8(b)–(d), when the spin rate is higher than 1000 rpm, larger three-phase zones are exposed to the ambient in the micro- and nano-electrodes. The cathodic generated water could be evaporated soon; therefore, cathodic reaction is continued

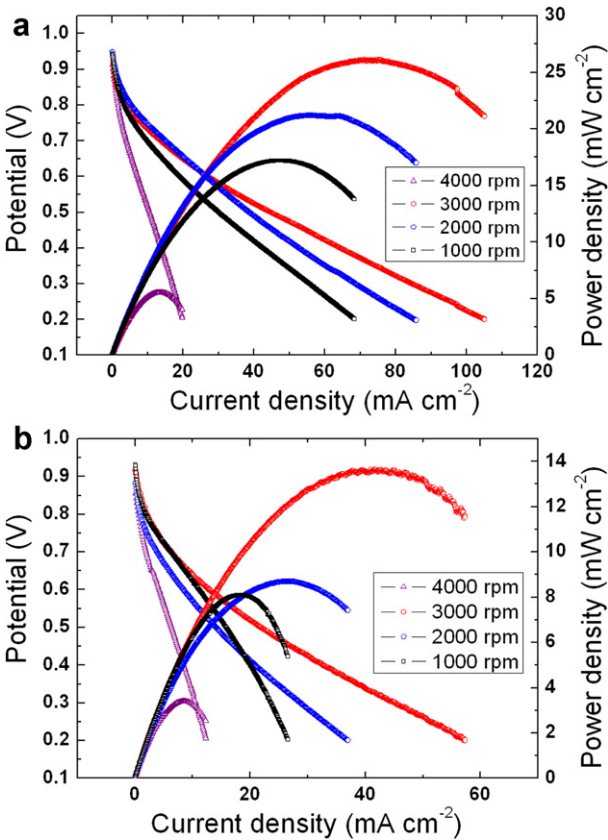


Fig. 13. The polarization curves of the μ -PEMFCs with different ionomer spinning-in conditions at the cathodes; (a) active testing condition, and (b) passive testing condition. The black square, blue pentagon, red hexagon and purple triangle represent the spinning-in conditions of 1000, 2000, 3000, and 4000 rpm, respectively. (For interpretation of the references to color in this figure legend, the reader is referred to the web version of this article.)

without limitations even at a high current density of 58 mA cm^{-2} (3000 rpm spinning-in condition).

However, under the passive testing for 1000 rpm spinning-in condition, the concentration polarization can be observed. Since most of the three-phase zones are buried inside the ionomer layer at this condition, the reaction sites could quickly be covered and inactivated by the cathodic product, H_2O , and the concentration polarization could therefore be observed.

The trend of peak power densities also follows the CV and EIS results, and the spinning-in condition of 3000 rpm also shows the best performance. The best peak power densities are 26 and 13.6 mW cm^{-2} , for active and passive testing systems, respectively. Finally, we summarize the performance of the present micro-fuel cells [1–8] and compare them with the current study in Table 1, revealing that the current study provides a high performance micro-fuel cell system. Especially the catalyst utilization ratios for 3000 rpm spinning-in condition reach 38.2 and $20 \text{ W g}_{\text{Pt}}^{-1}$ for active and passive testing systems, respectively, which are superior to all of the present studies and evidence that the cathodic efficiency, catalyst utilization ratio and peak power density of micro-fuel cell systems can be improved by using the unique process introduced in this study.

4. Conclusion

In this study, a high performance micro-PEM fuel cell is introduced. The performance is improved by three mechanisms incorporated in a micro-fuel cell, including the integration of micro- and nano-structures to carry out larger reaction surface areas, the reduction of oxygen diffusion impedance by ultrathin ionomer coating in three-phase zones, and the improvement of interfacial strength by micro-interlocks for fuel cell packaging. The best cell

peak power density is 26 mW cm^{-2} , which corresponds to a catalyst utilization ratio of $38.2 \text{ W g}_{\text{Pt}}^{-1}$ demonstrating a high performance micro-PEM fuel cell system.

Acknowledgments

The authors would like to thank National Science Council of Taiwan for the financial support (NSC 100-3113-E-007-001).

References

- [1] K. Shah, W.C. Shin, R.S. Besser, J. Power Sources 123 (2003) 172–181.
- [2] Y. Zhang, J. Lu, H. Zhou, T. Itoh, R. Maeda, J. Microelectromech. Syst. 17 (2008) 1020–1028.
- [3] K.B. Min, S. Tanaka, M. Esashi, J. Micromech. Microeng. 16 (2006) 505–511.
- [4] S.C. Kelley, G.A. Deluga, W.H. Smyrl, AIChE J. 48 (2002) 1071–1082.
- [5] J. Yeom, G.Z. Mozsgai, B.R. Flachsbarth, E.R. Choban, A. Asthana, M.A. Shannon, P.J.A. Kenis, Sens. Actuators B 107 (2005) 882–891.
- [6] J. Yeom, R.S. Jayashree, C. Rastogi, M.A. Shannon, P.J.A. Kenis, J. Power Sources 160 (2006) 1058–1064.
- [7] Z. Xiao, G. Yan, C. Feng, P.C.H. Chan, I.M. Hsing, J. Micromech. Microeng. 16 (2006) 2014–2020.
- [8] Y.H. Seo, Y.H. Cho, Sens. Actuators A 150 (2009) 87–96.
- [9] W.R. Chang, J.J. Hwang, F.B. Weng, S.H. Chan, J. Power Sources 166 (2007) 149–154.
- [10] H.C. Peng, H.S. Khoo, F.G. Tseng, Jpn. J. Appl. Phys. 51 (2012) 027302.
- [11] K. Furukawa, K. Okajima, M. Sudoh, J. Power Sources 139 (2005) 9–14.
- [12] H. Yamada, T. Hirai, I. Moriguchi, T. Kudo, J. Power Sources 164 (2007) 538–543.
- [13] Y.S. Wu, S.M. Gong, C.H. Wang, T.K. Yeh, M.C. Tsai, C.H. Tsai, Y.C. Su, F.G. Tseng, Electrochim. Acta 64 (2012) 162–170.
- [14] H.C. Peng, C.C. Cheing, F.G. Tseng, Proceedings of PowerMEMS microEMS2008, Sendai, Japan, Nov. 9–12, 2008, pp. 31–34.
- [15] K. Jiao, X. Li, Prog. Energy Combust. 37 (2011) 221–291.
- [16] P. Choi, N.H. Jalani, R. Datta, J. Electrochem Soc. 152 (3) (2005) E123–E130.
- [17] M. Ciureanu, R. Roberge, J. Phys. Chem. B 105 (2001) 3531–3539.
- [18] D.C. Huang, P.J. Yu, F.J. Liu, S.L. Huang, K.L. Hsueh, Y.C. Chen, C.H. Wu, W.C. Chang, F.H. Tsau, Int. J. Electrochem. Sci. 6 (2011) 2551–2565.